 

# Investigation of Reynolds Number Scale Effects on Propeller Tip Vortex Cavitation and Propeller-Induced Hull Pressure Fluctuations

Roland Gosda*, Stephan Berger and Moustafa Abdel-Maksoud

*Institute for Fluid Dynamics and Ship Theory, Hamburg University of Technology, Hamburg, Germany*

**Abstract**

A two-dimensional viscous vortex model with a cylindrical cavity at its center is applied to investigate Reynolds number scale effects on propeller tip vortex cavitation. First, the behaviour of small isolated cavities inside the viscous core are studied. In order to study Reynolds number scale effects, the viscous core radius of the vortex is varied. Thereafter, the investigation is extended to the cavitating tip vortex of a propeller as a whole. A generic scenario is set up which is representative for real propeller flows. It can be shown that apart from the viscous core radius, the blade load and the presence of sheet cavitation influence hull pressure fluctuations due to tip vortex cavitation in a significant manner.

**Keywords**: Tip Vortex Cavitation, Marine Propellers, Cavitation-Induced Noise and Vibration

## 1 Introduction

Propeller tip vortex cavitation is known to contribute to underwater noise and extended hull pressure fluctuations. In practice, the assessment of the propeller's cavitation behaviour is usually carried out by means of model tests, i.e. a geometrically similar model of propeller and ship with a scale factor of, say, $1/40 \ldots 1/25$ is investigated. Due to Reynolds number scale effects, extrapolating the results to the full-scale propeller is then afflicted with some uncertainties. In the present work, some light shall be shed on these uncertainties. Two aspects are considered to have a great impact:

(1) There is a correlation between the viscous core radius of the trailing tip vortex and the boundary layer thickness of the lifting surface [1], i.e. the propeller blade. Assuming typical operation conditions and length dimensions for model tests, the viscous core radius of the tip vortex of the model propeller can be up to 60 % relatively larger than the full-scale pendant [3]. This certainly will have an effect on the dynamic behaviour of the cavities inside the vortex core.

(2) The propeller operates in the ship's wake field, which in turn is highly affected by the different Reynolds numbers of model and ship. Since the unsteady propeller load depends on the inhomogeneous inflow, the circulation of the tip vortex and – if present – the extent of sheet cavitation at the propeller blade tip will also be influenced accordingly. These factors are assumed to have a considerable impact on the dynamical behaviour of tip vortex cavitation.

In the present paper, both effects are discussed and separated from each other. The numerical simulations carried out for this purpose are based on a two-dimensional vortex model, where the behaviour of a cylindrical cavity in the center of a viscous line vortex is observed. In order to capture the interaction between cavity and vortical flow, the method solves both the circumferential as well as the radial momentum equation in a coupled manner.

The paper is organised as follows: After introducing the governing equations of the model and making some notes on the numerical implementation in Sections 2 and 3, the focus in Section 4 is put on point (1) mentioned above by carrying out an extensive numerical study for cylindrical bubbles in the viscous core of a line vortex at various Reynolds numbers and initial conditions. Finally, in Section 5, a simplified generic test scenario is set up in order to elucidate those scale effects subsumed under point (2).

## 2 Governing Equations and Boundary Conditions

Modelling a viscous line vortex with a cylindrical cavity at its center consists of an initial boundary value problem of a set of coupled partial differential equations. As derived in [6] or [8] for example, the equations are the Rayleigh-Plesset equation (integral form of the radial momentum equation)

$$\left(\ddot{r}_c r_c + \dot{r}_c^2\right) \ln\left(\frac{r_D}{r_c}\right) + \frac{\dot{r}_c^2 r_c^2}{2}\left(\frac{1}{r_D^2} - \frac{1}{r_c^2}\right) = \frac{1}{\rho}\left(p_v + p_{g,\mathrm{ref}}\left(\frac{r_{c,\mathrm{ref}}}{r_c}\right)^2 - 2\mu\frac{\dot{r}_c}{r_c} - \frac{S}{r_c} - p_D\right) + \int_{r_c}^{r_D} \frac{v_\varphi^2}{r}\,\partial r \quad (1)$$

*Corresponding author, contact: roland.gosda@tuhh.de

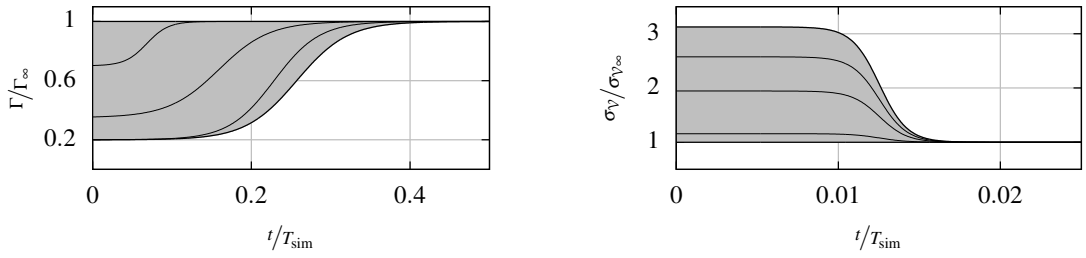


**(a)** Ciculation $\Gamma$. **(b)** Cavitation number $\sigma_\mathcal{V}$.

**Figure 1:** Ranges and evolution of the circulation $\Gamma$ and cavitation number $\sigma_\mathcal{V}$ over time $t$ with respect to the duration of the simulation $T_{\text{sim}}$. $\Gamma_\infty$ and $\sigma_{\mathcal{V}\infty}$ denote the final circulation and cavitation number, respectively. While the thick lines show the limits for possible slopes, the thin lines hint randomly varying slopes.

and the circumferential equation of momentum

$$\rho\left(\frac{\partial v_\varphi}{\partial t}+\frac{\dot{r}_c r_c}{r}\frac{\partial v_\varphi}{\partial r}+\frac{\dot{r}_c r_c}{r^2}v_\varphi\right)=\mu\left(\frac{\partial^2 v_\varphi}{\partial r^2}+\frac{1}{r}\frac{\partial v_\varphi}{\partial r}+\frac{1}{r^2}v_\varphi\right)+f_\varphi, \tag{2}$$

where the kinematic relation $v_r r=\dot{r}_c r_c$ has been used. Here, $v_\varphi$ denotes the circumferential velocity, $v_r$ the radial velocity, and $r_c$ is the cavitation radius with its respective derivatives in time $\dot{r}_c$ and $\ddot{r}_c$. A large arbitrary outer domain radius $r_D$ is required for modelling the radial equation of momentum. Further constants and variables are: the density $\rho$, the partial vapour saturation pressure $p_v$, the tuple $\{p_{g,\text{ref}}, r_{c,\text{ref}}\}$ regarding the non-condensable gaseous content inside the cavity, the pressure $p$, the interface tension coefficient $S$, the viscosity $\mu$, the radial coordinate $r$ and the time $t$. The use of the momentum source term $f_\varphi$ will be explained later. The spatial domain is bounded by $r\in[r_c, r_D]$. The boundary conditions for (2) are:

$$\begin{aligned}\frac{\partial v_\varphi}{\partial r}-\frac{v_\varphi}{r}=0, \text{ at } r=r_c>0,\\ v_\varphi(r_c)=0, \text{ if } r_c=0,\end{aligned} \tag{3}$$

stating that no shear forces act across the liquid-vapour interface. Furthermore, $v_\varphi(r\geq r_D)=\frac{r_D}{r}v_\varphi(r_D)$ is used as an approximation for the velocity field outside the domain.

## 3 Numerical Implementation

The set of governing equations (1) and (2) is solved using finite differences and a Crank-Nicolson-scheme as suggested by [5], while the spatial domain is transformed to a uniform grid as described in [8]. For previous results and validation, please refer to [2, 3].

## 4 Reynolds Number Effects on an Isolated Vortex Cavity

In the following, the behaviour of small cavitation bubbles in the viscous core of a propeller tip vortex is studied. There are two significant simplifications: (1) the three-dimensional character of the flow is neglected, i.e. cylindrical 'bubbles' are considered, and (2) these bubbles are located in the center of the vortex, whereas the passage to the vortex center is not taken into account. Despite these simplifications, some important conclusions can be drawn from this scenario.

Predominant parameters governing the tip vortex flow are the circulation $\Gamma$ of the tip vortex, which increases due to the roll-up process, the ambient pressure $p_D$, which may also undergo changes, as well as the viscous core radius $r_a$, in which Reynold number scale effects are assumed to be reflected.

To study the influence of the different parameters, 10000 simulations of single bubbles have been carried out. A characteristic quantity of the problem is the vortex cavitation number $\sigma_\mathcal{V}$, which is defined here as

$$\sigma_\mathcal{V}=\frac{p_D-p_v}{1/2\rho\mathcal{V}_\Gamma^2} \text{ with } \mathcal{V}_\Gamma=\frac{\Gamma_\infty}{2\pi r_D} \tag{4}$$

and $r_D$ being the outer domain radius introduced in Section 2. The initial data has been chosen s.t. Reynolds number effects of the core radius are included by selecting discrete values ${}^{r_{a0}}/_{r_D}\in\{0.02, 0.04, \ldots, 0.2\}$. Furthermore, the increase of circulation and changes in the ambient pressure $p_D$ as the bubble travels downstream along

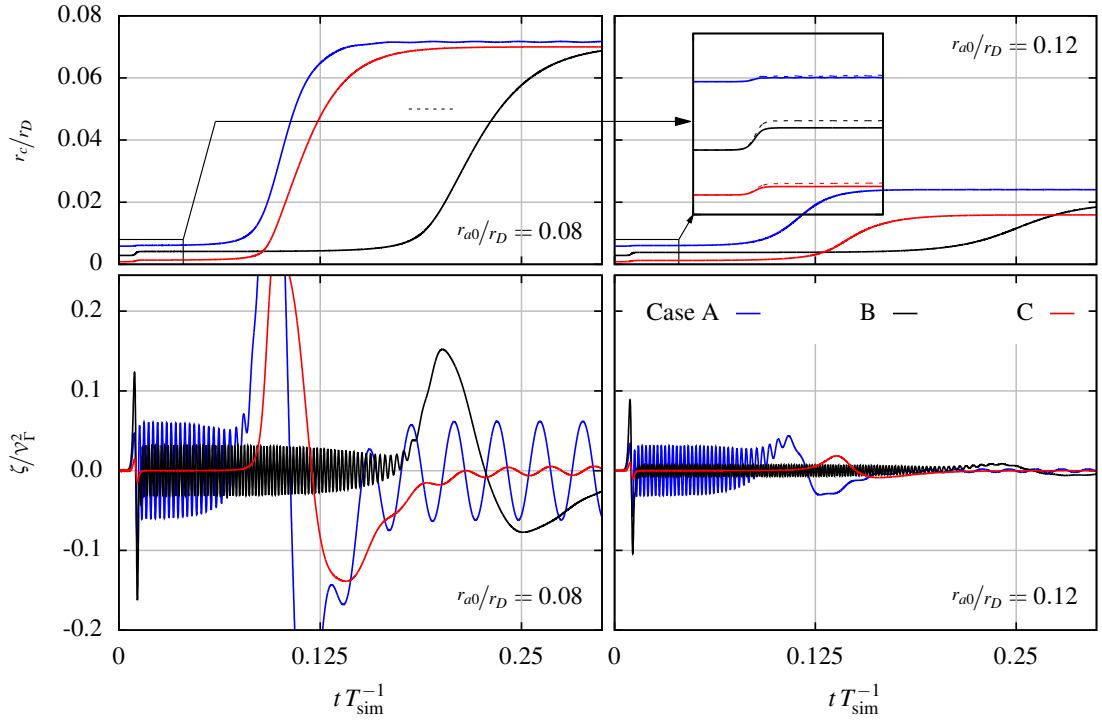


**Figure 2:** Three exemplary bubble evolutions for the cases listed in the table below for $r_{a0}/r_D = 0.08$ (left) and $r_{a0}/r_D = 0.12$ (right) resembling full-scale and model conditions, respectively. Top: evolution of the cavity radius $r_c(t)$; bottom: pseudo radiated pressure $\zeta$ (see text for definition).

| Case | Colour | $r_{c0}/r_D$ | $r_{a0}/r_D$ | $t/T_{\text{sim}}$ when $\Gamma \geq$ | | $\sigma_{\mathcal{V}0}/\sigma_{\mathcal{V}\infty}$ |
|---|---|---|---|---|---|---|
| | | | | $105\,\%\,\Gamma_0$ | $99\,\%\,\Gamma_\infty$ | |
| A | • blue | $5.870 \cdot 10^{-3}$ | 0.08, 0.12 | 0.080 | 0.226 | 1.048 |
| B | • black | $2.852 \cdot 10^{-3}$ | 0.08, 0.12 | 0.182 | 0.478 | 1.641 |
| C | • red | $8.658 \cdot 10^{-4}$ | 0.08, 0.12 | 0.058 | 0.278 | 1.814 |

The magnifying glass in the upper right diagram helps to observe the impact of the change of the cavitation number $\sigma_\mathcal{V}$ from $\sigma_{\mathcal{V}0}$ to $\sigma_{\mathcal{V}\infty}$. Within the magnifying glass, the solid lines correspond to $r_{a0}/r_D = 0.12$, whereas the dashed lines display the results for $r_{a0}/r_D = 0.08$. The influence of the viscous core radius is relatively small at this stage.

the vortex axis are varied randomly in intervals $\Gamma_0/\Gamma_\infty \in [0.2, 1.0]$ and $\sigma_{\mathcal{V}0}/\sigma_{\mathcal{V}\infty} \in [1.0, 3.0]$, respectively, using an uniform distribution, while the initial cavitation radius is chosen to be in the range of $r_{c0}/r_D \in [2 \cdot 10^{-5}, r_{a0}/r_D]$. Here, subscripts with $(\cdot)_0$ denote respective parameters at $t_0$, i.e. at the initialisation of the simulation, whereas $(\cdot)_\infty$ refers to the final state of a simulation.

Both the increase of circulation and the drop of pressure have been prescribed using a hyperbolical tangent (see Figure 1). The initial circumferential velocity $v_\varphi(r)$ is modelled using the analytical model proposed by [4] – basically a modified Burgers vortex-like radial distribution of circumferential velocity. Thus, $r_{a0}$ refers to the core radius of the non-cavitating vortex. In order to mimic the increase of circulation, the momentum source term $f_\varphi$ of the circumferential momentum equation (2) is manipulated according to the prescribed increase of circulation. All simulations have been initialised with a corresponding partial pressure of the non-condensable gaseous content $p_{g,\text{ref}}$ s.t. the cavity is in equilibrium at $t_0$.

Exemplary simulation results are shown in Figure 2 for the three cases A, B and C and two viscous core radii. In the figure, the evolution of the cavity radius $r_c(t)$ is shown in the upper diagrams, and the pseudo radiated pressure resulting from the oscillation of the cavity radius in terms of

$$\zeta \equiv \frac{\partial^2 \left(r_c^2\right)}{\partial t^2} \tag{5}$$

is plotted in the lower diagrams. These three cases demonstrate the strong dependence of the evolution of the bubble radius on the initial conditions and the viscous core radius. It can be observed that in the present scenario, a bubble undergoes three phases. The first phase starts directly after the pressure drops from $p_{D0}$ to $p_{D\infty}$, and the third phase is characterised by the steady state oscillations arising when the vortex circulation $\Gamma$ reaches its final

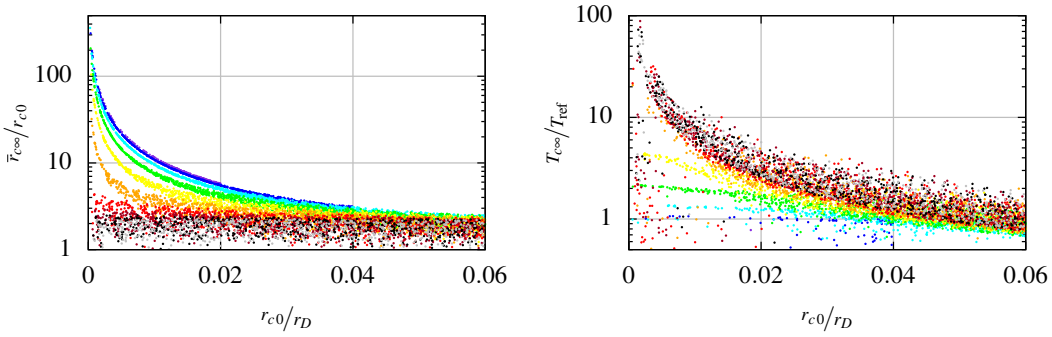


**(a)** Mean cavitation radius $\bar{r}_{c\infty}$.

**(b)** Oscillation period $T_{c\infty}$.

**Figure 3:** Exemplary simulation results with respect to oscillation period $T_{c\infty}$ and mean cavitation radius $\bar{r}_{c\infty}$ at the end of the simulation. Each dot indicates one simulation result. Colour code: $r_{a0}/r_D = \{\bullet\ 0.02, \bullet\ 0.04, \bullet\ 0.06, \bullet\ 0.08, \bullet\ 0.1, \bullet\ 0.12, \bullet\ 0.14, \bullet\ 0.16, \bullet\ 0.18, \bullet\ 0.2\}$.

value. The second phase refers to the transition from the first to the third phase. In the following, the steady-state results of the third phase will be analysed.

Figure 3(a) shows the average cavitation radius $\bar{r}_{c\infty}$ of the steady-state oscillations. Obviously, a larger viscous core radius $r_a$ dampens the growth of the cavitation radius $\bar{r}_{c\infty}/r_{c0}$. For large cavitation radii, the results for cases with different core radii merge, which is due to the increasing similarity to the inviscid solution that starts to dominate the viscous effects.

The results presented in Figure 3(b) show the effect of $r_{c0}$ on the oscillation period $T_{c\infty}$ in the steady state with respect to the linearised inviscid oscillation period [7]:

$$T_{\mathrm{ref}} = 4\pi^2 \bar{r}_{c\infty}^2 \Gamma_\infty^{-1} \sqrt{\ln\left(r_D \bar{r}_{c\infty}^{-1}\right)}. \tag{6}$$

The deviance of the oscillation period $T_{c\infty}$ to the reference period $T_{\mathrm{ref}}$ is more dominant if $r_{a0}$ is larger and if the relative difference of the initial cavitation radius $r_{c0}$ to $r_{a0}$ is large. This emphasises the effect that the viscous core has: A larger viscous core radius effectively slows down bubble oscillations.

In the following, the implications on hull pressure fluctuations due to a cavitating propeller tip vortex are investigated.

## 5 Reynolds Number Effects on a Generic Propeller Tip Vortex

So far, the behaviour of isolated vortex cavities ('bubbles') has been studied. In this section, Reynolds number scale effects on the behaviour of a cavitating propeller tip vortex as a whole are considered. The applied model originates from [9, 10] and is described in detail in [2, 3]. It considers the propeller tip vortex to be a large sequence of vortex segments. Each of them is treated separately by the method used so far in this paper. The scheme is shown in Figure 4. A segment $k$ originates at the propeller tip at $t = t_{0,k}$. According to the selected time step size $\mathrm{d}t$, each element has the length $\mathrm{d}l_k = \mathrm{d}l = \mathrm{d}t\left((\pi n D)^2 + V_s^2\right)^{0.5}$, where $n$ is the number of revolutions, $D$ is the propeller diameter and $V_s$ is the ship speed. The segment $k$ is swept away by the flow making room for the new segment $k+1$ originating at the propeller tip at $t = t_{0,k+1}$. In order to approximate the tip vortex roll-up, the circulation $\Gamma_k^\star\left(t_{0,k}, t^\star\right)$ assigned to the segment grows from an initial value $\Gamma_k^\star\left(t_{0,k}, 0\right) = \gamma_{\mathrm{ini}}\Gamma_b\left(t_{0,k}\right)$ to $\Gamma_k^\star\left(t_{0,k}, t^\star\right) = \Gamma_b\left(t_{0,k}\right)$ as the segment travels downstream and the segment's age $t^\star$ exceeds a certain value. Apart from the circulation, the initial viscous core radius $r_{a0}$ of the tip vortex and the initial cavitation radius $r_{c0,k}$ of a segment $k$ at $t = t_{0,k}$ are governing influence parameters of the problem.

Once the unsteady cavitation radius $r_c$ is known for every segment, the unsteady pressure $p'_{\mathrm{TV}}$ due to the cavitation volume fluctuation of the tip vortex observed in a point $O$ sufficiently far away from the propeller can be approximated by the linearised Bernoulli equation:

$$p'_{\mathrm{TV}} = -\rho \frac{\partial \Phi_{\mathrm{TV}}}{\partial t}, \tag{7}$$

where $\Phi_{\mathrm{TV}} = \Phi_{\mathrm{TV}}(t) = \sum_k \phi_k^\star$ is the accumulated potential of all segments $k$ with

$$\phi_k^\star = -\frac{\sigma_{c,k}^\star}{4\pi d_k} \quad \text{and} \quad \sigma_{c,k}^\star = \pi \mathrm{d}l \frac{\partial\left(r_{c,k}^2\right)}{\partial t}. \tag{8}$$

 

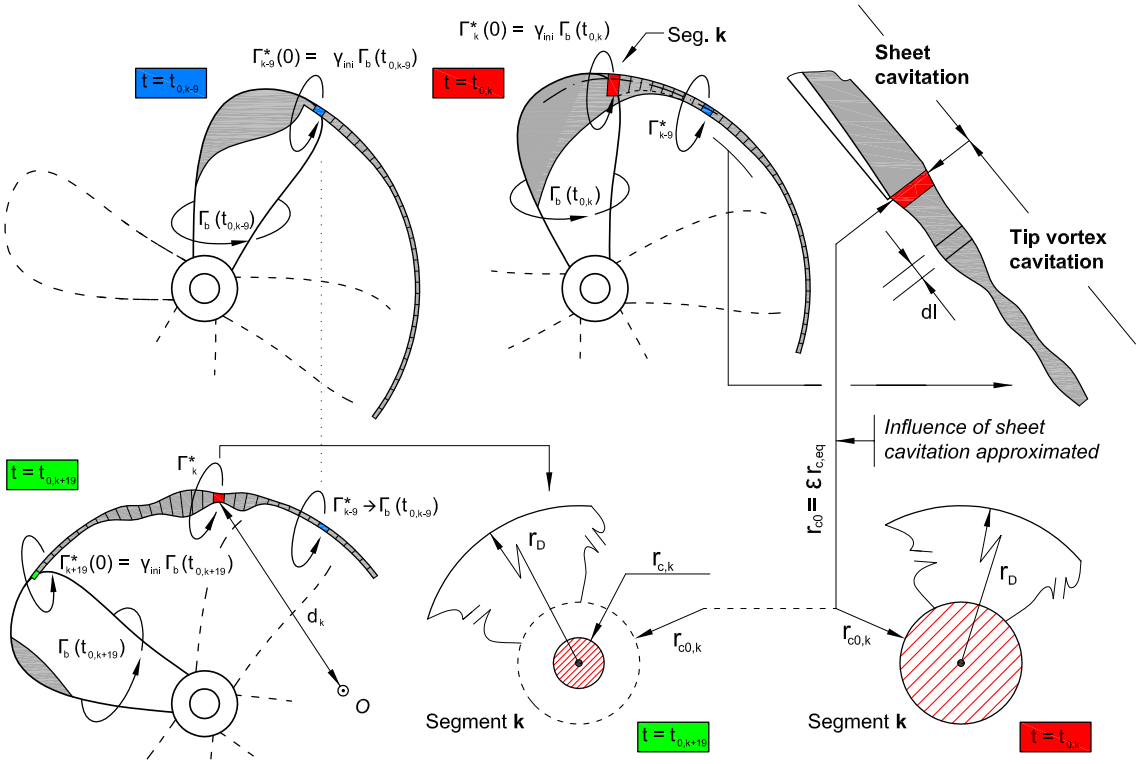


**Figure 4:** Segmentation scheme of the propeller tip vortex cavitation model. Also showing the influence of sheet cavitation on the dynamic behaviour of tip vortex cavitation.

In order to study Reynolds number effects on pressure fluctuations on the ship hull caused by the cavitating tip vortex, a generic scenario has been developed that reproduces the flow conditions observed at real propeller–hull configurations and covers both effects (point 1 and 2) mentioned in the introduction in Section 1. First, consider the circulation $\Gamma_b$ bound to the blade as shown for one revolution in the upper diagram of Figure 5a. Here, $\vartheta = 0°$ and $\vartheta = 360°$, respectively, refer to the 12 o'clock-position in the wake field where the velocity deficit due to the ship hull's boundary layer is maximum. The black curve refers to full-scale conditions. In order to arrive at the conditions for the model (represented by the dashed red curve), the plateau of high blade load has been broadened according to the more pronounced wake peak one would expect for model conditions, and the maximum at 0° has been increased slightly for the same reason. In both cases, the average propeller thrust is the same. For the sake of simplicity, it is assumed that the initial circulation of the tip vortex directly behind the trailing edge is half of the circulation bound to the blade, i.e. $\gamma_{\text{ini}} = 0.5$.

Sheet cavitation in the propeller tip region is assumed to excite pressure fluctuations induced by the tip vortex by widening the vortex cavity beyond the equilibrium cavity radius, such that oscillations of the cavitation radius are stimulated. This phenomenon will usually be observed in the wake peak region and is discussed in [2, 3]. To approximate this effect without modelling sheet cavitation, the initial cavitation radius $r_{c0}$ of a new tip vortex segment is chosen to be the equilibrium cavitation radius $r_{c,\text{eq}}$ for given flow conditions which is then exaggerated by a factor $\varepsilon \in [1.0, \varepsilon_{\max}]$ in the wake peak region. In the generic scenario investigated here, the following procedure is used:

$$r_{c0} = \begin{cases} \varepsilon r_{c,\text{eq}} & \text{in the wake peak region} \\ r_{c,\text{eq}} & \text{elsewhere} \end{cases} \tag{9}$$

with $r_{c,\text{eq}}$ at $t = t_0$ for every segment $k$ and given tip vortex flow conditions (see lower diagram of Figure 5a).

In Figure 5b, exemplary pressure signals $p'_{\text{TV}}$ are shown in the frequency domain for two extreme cases in a dimensionless manner in terms of $k_{\hat{p}} = \hat{p}_{\text{TV}}/(\rho n^2 D^2)$ and $f/f_b$ with the blade frequency $f_b = nn_b$. Obviously, pressure fluctuations are predicted to be less intense under model conditions than under full-scale conditions. To clarify this further, the influence of the viscous core radius and the exaggeration factor $\varepsilon_{\max}$ on pressure fluctuations $k_{\hat{p}^{[3]}}$ and $k_{\hat{p}^{[4]}}$ of third and fourth order, i.e. occurring with $3f_b$ and $4f_b$, has been studied. The results are shown in Figure 6.

Obviously, the amplitudes of pressure fluctuations due to tip vortex cavitation generally grow with the exag-

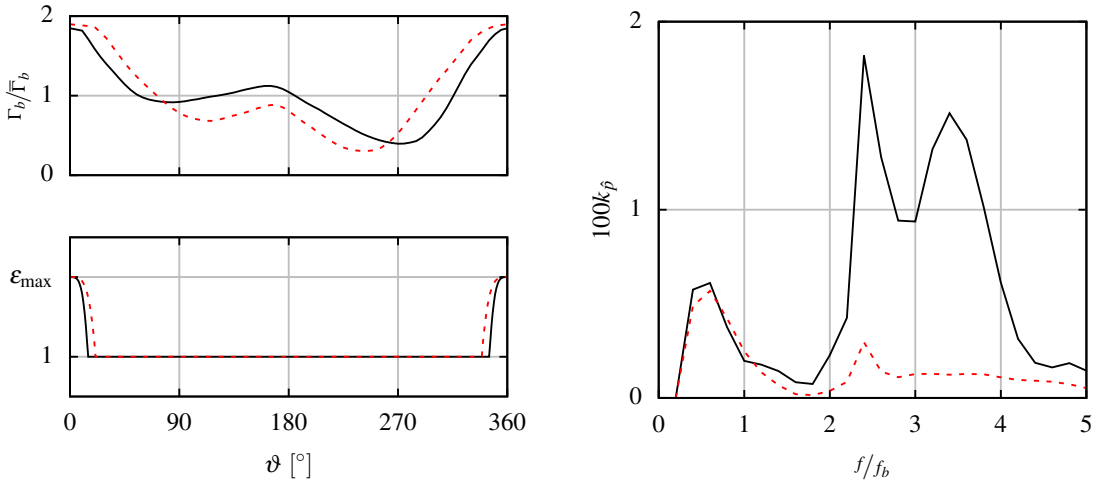


**(a)** $\Gamma_b$ and $\varepsilon$ over $\vartheta$ for full-scale and model configuration.

**(b)** Exemplary pressure amplitude spectra.

**Figure 5:** Circulation distributions $\Gamma_b(\vartheta)$ and exaggeration factors $\varepsilon(\vartheta)$ (a) and exemplary pressure amplitude spectra due to tip vortex cavitation (b) for representative full-scale (solid line) and model configurations (dashed line) with $\varepsilon_{\max} = 1.225$ and $2 \cdot 100\, r_{a0}/D = \{\bullet\ 1.067, \bullet\ 1.867\}$, respectively. These extreme cases are also included in the diagrams displayed in Figure 6 using filled circles with the same colour code.

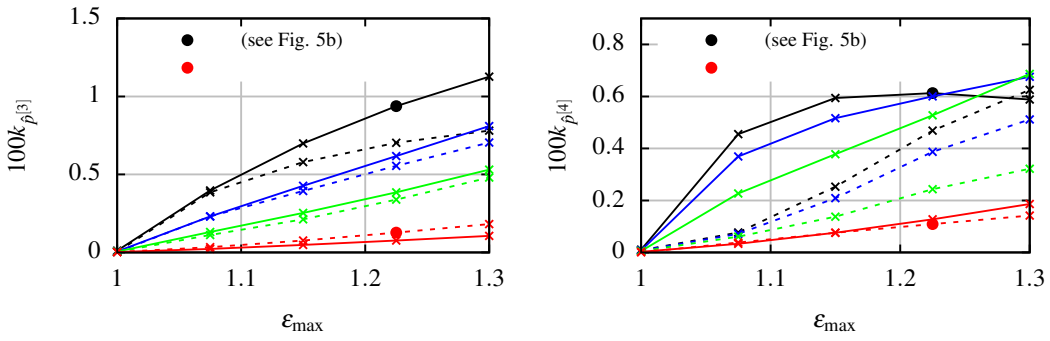


**(a)** Third order $f = 3f_b$.

**(b)** Fourth order $f = 4f_b$.

**Figure 6:** Influence of the viscous core radius $r_{a0}$ and the exaggeration factor $\varepsilon_{\max}$ for the full-scale configuration (solid lines) and the model configuration (dashed lines). Colour code: $2 \cdot 100\, r_{a0}/D = \{\bullet\ 1.067, \bullet\ 1.333, \bullet\ 1.6, \bullet\ 1.867\}$. The filled circles correspond to the exemplary cases in Figure 5b.

geration factor $\varepsilon_{\max}$ and – similar to the observation made in the previous section – a larger viscous core radius dampens pressure fluctuations. No significant pressure fluctuations are induced if sheet cavitation is not present, i.e. $\varepsilon_{\max} = 1.0$. However, it is important to note that, apart from this, the angular distribution of blade load in terms of $\Gamma_b(\vartheta)$ can have a significant impact on the results.

## 6 Discussion, Conclusions and Future Outlook

In the present paper, Reynolds number scale effects on tip vortex cavitation have been investigated by means of a method which is based on the model of a cavitating axisymmetrical viscous line vortex. The important interaction between the distribution of circumferential velocity $v_\varphi(r)$ and the cavity inside the vortex is captured by the present method. With respect to isolated vortex cavities (cylindrical 'bubbles') inside the viscous core of the vortex, it has been shown in Section 4 that a larger viscous core radius effectively dampens both the growth of the cavity radius and the frequency of its oscillations.

The problem gets more complex when pressure fluctuations radiated by the propeller tip vortex as a whole are addressed. Apart from the viscous core radius, which tends to dampen oscillations as it is increased, the blade load in the wake peak region around the 12 o'clock-position and sheet cavitation at the blade tip also influence pressure fluctuations in a significant manner. Within the simulations carried out, the latter has been taken into account by a

simplified model. More knowledge is required about the complex and relevant cavitation pattern in the blade tip region, which is characterised by the transition from sheet cavitation to tip vortex cavitation.

With respect to hull pressure fluctuations due to cavitating propellers, the results obtained can be valuable to better extrapolate model test results to the full-scale ship. Further investigations are required to obtain a reliable general rule for the extrapolation.

**Acknowledgements**

The authors would like to thank the German Federal Ministry for Economic Affairs and Energy for the financial support within the research projects NoiseLES-eNoiSim and HiOcav-HiOsim.

**References**

[1] R. E. A. Arndt: *Vortex Cavitation*. Fluid Vortices. Springer, Dordrecht, 1995. 731–782.

[2] S. Berger, R. Gosda, M. Scharf, R. Klose, L. Greitsch, M. Abdel-Maksoud: *Efficient Numerical Investigation of Propeller Cavitation Phenomena Causing Higher-Order Hull Pressure Fluctuations*. 31st Symposium on Naval Hydrodynamics, Monterey, California, 2016.

[3] S. Berger: *Numerical Analysis of Propeller-Induced Higher-Order Pressure Fluctuations on the Ship Hull*. PhD Thesis, Hamburg, 2017 (`https://doi.org/10.15480/882.1605`).

[4] J. Bosschers: *On the influence of viscous effects on 2-D cavitating vortices*. Journal of Hydrodynamics, Ser. B 22.5, 2010.

[5] G.L. Chahine: *Bubble interactions with vortices*. Fluid Vortices. Springer, Dordrecht, 1995. 783-828.

[6] J. Choi, C. Hsiao, G. Chahine, S. Ceccio: *Growth, oscillation and collapse of vortex cavitation bubbles*. Journal of Fluid Mechanics, Cambridge University Press, 2009.

[7] J.-P. Franc, J.-M. Michel: *Vortex Cavitation*. Fundamentals of Cavitation. Kluwer Academic Publishers, 2004. 223–246.

[8] R. Gosda: *Numerical Investigation of the Interaction between a Viscous Line Vortex and a Cylindrical Cavitation Bubble in the Viscous Core Region*. Bachelor thesis, Hamburg University of Technology, 2015; ( `www.panmare.de` → Publications → 2016).

[9] T. Kanemaru, J. Ando: *Numerical Analysis of Tip Vortex Cavitation on Marine Propeller Using a Simple Surface Panel Method SQCM*. Fourth International Symposium on Marine Propulsors, Austin, Texas, 2015.

[10] J. Szantyr: *A Computational Model of Propeller Cavitating Tip Vortex Interacting with the Rudder*. CAV2006, Wageningen, Netherlands, 2006.